Satellite Microwave Radar- and Ihtoy-tracked Ice Motion in the Weddell Sea during WWGS '92

Mark R. Drinkwater
Jet Propulsion I aboratory, California Institute of Technolog', 4800 Oak Grove Drive
Pasadena, California 91109 USA. ph: (818) 354-818 fax: (818) 393-6720

Christoph Kottmeier
Alfred Wegener Institut für Polar- und Meeresforschung, Am Handelshafen 12
1>-2850 Bremerhaven, Germany. ph: 49 (471) 4831-250 fax: 49 (471) 4831-425

A bstract The first results of ERS-1 SAR sea-ice drift tracking are presented for Antarctica. Summer and Winter examples illustrate temporal variations in ice drift in the Western and Eastern Weddell Sea during two field experiments. Time-series of mean drift velocity, divergence and rotation are compared with meteorological data from an ice camp and by instrumented buoys. Results indicate that SAR successfully characterizes the 'spatially mesoscale' kinematics of Weddell Sea ice during summer and winter, providing that coverage, and temporal and spatial sampling are judiciously planned. Measurements show that winter ice production largely takes place during synoptic events where pulses of wind force ice divergence, lead formation and ice growth.

I. INTRODUCTION

Coupling between surface winds and Antarctic sea ice drives a large-scale gyre circulation in the Weddell Sea, and momentum transfer and the stress divergence causes fracturing and lead formations in the ice. Oceanographically, new-ice growth in leads results in a salt flux and salinization which can upset the marginal stability of the mixed layer and induce vertical convective events and ocean-atmosphere exchanges of large amounts of sensible heat and gases. Monitoring formation of this extensive Weddell Sea ice cover and estimation of the rate of ice production is critical to understanding the impact of the sea ice on horizontal and vertical thermohaline circulation patterns and the production of high salinity shelf and Antarctic b~ttom-water masses.

Until recently, passive microwave and visible wavelength images were the only source of lame-scale information on the sea-ice cover of the Southern"Ocean. With the launch of ERS-1, and the construction of two dedicated Antarctic receiving stations, it is now possible to record microwave radar images of the Bellingshausen, Weddell and Cosmonaut Seas. For the first time, all-weather, high resolution (-25 m) day and ni gt data are available for monitoring the surface characteristics of the Antarctic ice cover.

Antarctic images from ERS-1 Synthetic Aperture Radar (SAR) data enable tracking of ice motion. Data used in this study were recorded by the German Antarctic Receiving Station, and processed at the D-PAF. SAR images acquired during the 1992 drift of Ice Station Weddell (lSW-l), and the Winter Weddell Gyre Study (WWGS '92) are processed using an automatic algorithm to derive ice displacement vectors. Results are then compared with surface measurements made during the summer ISW-1 drift and by a 6-buoy array deployed during WWGS '92.

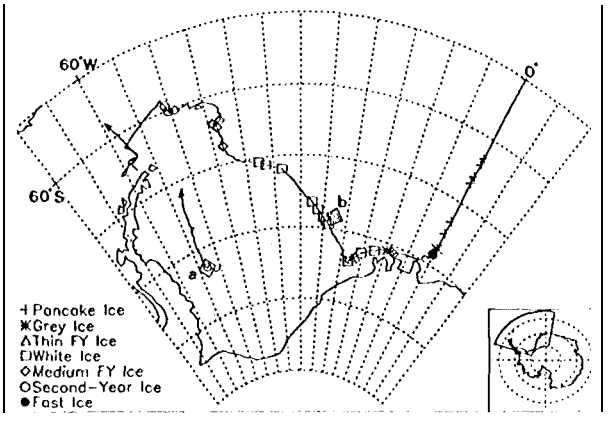

Figure 1. Weddell Sea map showing the drift track of ISW-1 and the transect of *Polarstern* during WWGS '92. Shaded boxes a. and b. identify locations of interest.

II. FIELD EXPERIMENTS

Two Antarctic field experiments took place in 1992 as part of the "AnZone" series of coordinated Southern-Ocean experiments. The first of these was the first manned drifting ice station in Antarctica. Ice Station Weddell, was deployed on an ice-floe platform carried northwards in the western limb of the Weddell Gyre (Gordon *et al.*, 1992). Its drift track is shown in Fig. 1 from deployment in early February through recovery in June, 1992, and a SAR image is shown in Fig. 2a characterizing Western Weddell Sea summer ice at location a. near the stint of the experiment. The 100 km scene, acquired on 7 February is dominated by large high-backscatter rounded floes surrounded by relatively dark open water. Contrast between the ice floes and the open water is variable across the image due to strong winds roughening and strengthening lead backscattering. Ice motion characteristics of this second-year ice pack are described later.

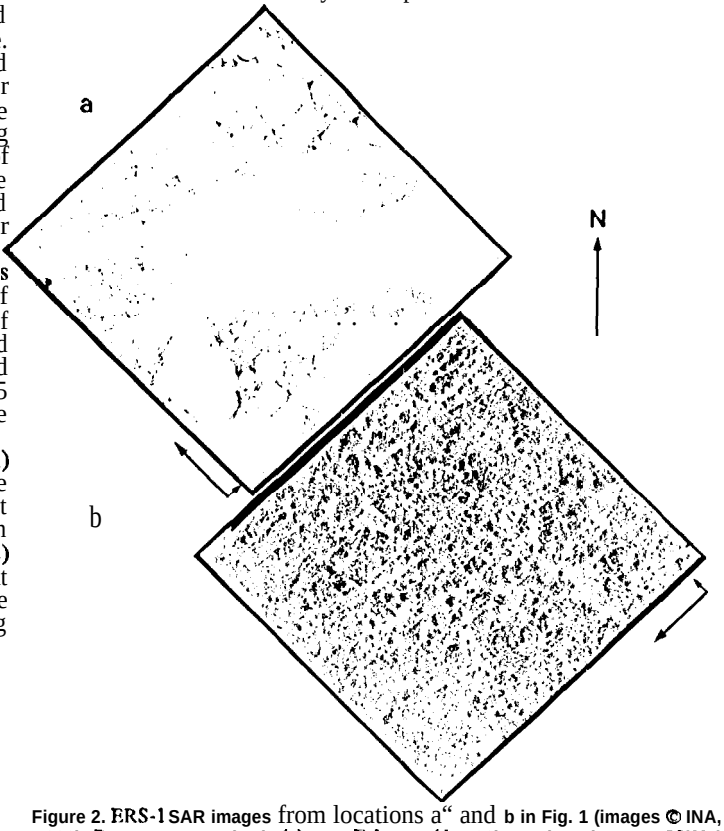

Figure 2. ERS-1 SAR images from locations a" and b in Fig. 1 (images © INA, 1992). Data were acquired; (a) on 7 February (day 38) at a location mar ISW-1 deployment; and (b) on 12 July (day 194) in the region of the WWGS '92 buoy array.

The Winter Weddell Gyre Study (WWGS '92), in contrast, was an austral winter shipborne experiment performed onboard R/V *Polarstern*. A plot of the icebreaker track is shown in Fig. 1, together with observations of the ice conditions en route. A predominantly pancake ice edge was encountered at 61°S O"W on June 12 and exited at 61°S 58"W on July 29, 1992. The SAR image in Fig. 2b characterizes the smooth white ice (young first-year ice) observed in the vicinity of location b. in Fig. 1. On 10 and 11 July, 1992, Argos buoys were deployed on six ice floes in this location, thus providing a valuable source of independent drift information with which to check SAR ice-tracking capability. Some preliminary comparisons arc made from this location in the following section.

111. SAR ICE-TRACKING RESULTS

Until ERS-1, tools with which to monitor Antarctic ice motion on a frequent basis were limited: no previous satellite SAR data were collected in the Weddell Sea, This research, using ERS-1 SAR data, has only recently demonstrated that algorithms, developed originally for tracking Arctic sea ice (Kwok *et al.*, 1990, 1991), can be applied with success in the Southern Ocean. SAR images used in this study were first geolocated and calibrated, and then processed using a modified ice-tracking algorithm which has filtering schemes optimized to account for differences in the appearance of Antarctic sea ice. Results of two separate investigations in the Western and Eastern Weddell Sea are described in the context of differing ice regimes and seasons and the motion in the Weddell Gyre.

Western Weddell Sea

The first set of examples characterise summer ice motion in a convergence zone where drift is constrained by the coast and forced northwards along the Antarctic peninsula. Sea ice is carried along by a combination of forcing by winds and a strong western boundary current concentrated along the shelf-break (Gordon *et al.*, 1992). Ice remaining in this location at the end of summer is identified in Fig. 1 as second-year ice and confirmed by physical measurements at ISW-1.

An example of SAR ice-tracking is shown in Fig. 3 for a period between an ascending and descending orbits on 15-16 February, 1992 (days 46-47). Ice displacement vectors are superimposed on the ISW-1 drift track where drift path turns from westwards to northwards: stars indicate recorded GPS locations of the ice camp closest to 11:34 and 04:27 GMT. The 5 km gridded vectors show close correspondence with the drift direction and displacement of ISW-1, but the mesoscale characteristics of the ice motion field vary considerably.

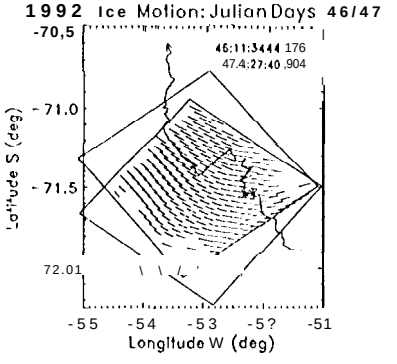

Figure 3. Summer ice-displacement vectors derived from two ERS-1 SAR images acquired at location a. in Fig. 1. at the dates and times given. An irregular solid line indicates the drift track of ISW-1.

Repeat passes over ISW-1 yield a time-series of data of the sea-ice drift around the ice camp. Figure 4 shows comparisons between measured winds (Fig. 4a) and the mean SAR-derived and GPS-measured drift speed of ISW-1 (Fig 4b). Until day 56, the ISW-1 meteorological tower was incomplete and daily winds are displayed: after day 56, a daily running mean of hourly wind measurements is used (original data shown as dotted line). Direct SAR observations of ISW were made on ascending orbits each 3 days, with some intermediate observations at 1 day intervals on descending orbits, Displacement fields such as Fig. 3 are derived for each interval between consecutive images and a time-series constructed. The mean drift speed is shown in Fig. 4b as straight-line segments with dotted error bars spaced at 1σ intervals. The IS W drift *record* is superimposed upon the SAR-derived drift speed with a record beginning on day 50. 'l'he ISW drift speed shows considerably more variance than the SAR image-averaged values extracted from the vector fields, although the SAR-derived values reproduce the underlying low-frequency trends of the ISW ice camp ftoc drift. Future comparisons will be made using single SAR vector magnitudes corresponding with the ISW locations. Surface winds are stronger at the start of the SAR record (Fig. 4a), settling down to a mean of ~5 m/s during the latter part. Ice drift responds accordingly, with both ISW and SAR-derived drift speeds exceeding 10 cm/s prior to day 50. Pulses in windspeed also result in rapid adjustments in ISW drift. A drawback is that the SAR revisit effectively filters out higher frequency motions of the ISW camp floe caused by tidal and inertial oscillations and other short-term motion.

A SAR product derived directly from the gridded displacement vectors is a table of partial derivatives of the x and y components of the velocity field. An image-wide mean divergence and rotation is computed directly from these results. Figure 4c and 4d show the SAR-derived mean divergence and rotation and the corresponding error bars at intervals of 1 standard deviation (1σ). Generally, the ice field undergoes net divergence during the early period of strong winds. In contrast, maximum convergence (Fig. 4c) occurs between days 50-52 after a period of calm. During this interval the winds increase quickly from 0.03 m/s up to 0.1 m/s, and the associated cyclonic weather system induces convergence in the ice cover, peaking at a mean of -1,28%/d over the imaging interval, Rotation in the ice field has a long-term mean value of zero, but maximum clockwise rotation (positive rotation) occurs between days 46 and 47 during maximum divergence and the highest drift rates. Also of note in Fig. 4d is the fact that the gridded ice motion data show a large degree of variation in the drift velocity field. Resulting mesoscale SAR measurements of divergence and rotation show a large variance about the mean, as illustrated by standard deviations of up to 10%/d for the divergence.

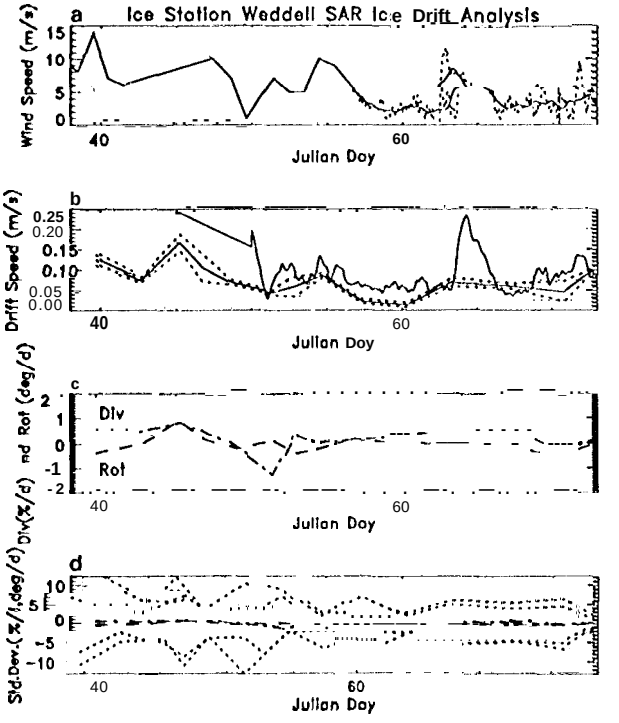

Figure 4. Comparison of ISW-1 drift data and SAR-derived ice motion Statistics: (a) wind speed **measured at ISW-1 (dotted** line indicates higher frequency met tower data); (b) mean **SAR** image-derived ice drift speed **with dotted lines at 1σ intervals, compared to ISW-measured drift speed; (c) SAR derived divergence and rotation (+ rotation = anti-clockwise); (d) 1 σ error bars for the divergence and rotation in (c).**

Eastern Weddell Sea

Preliminary winter results are shown for comparisons between buoy- and ERS-1 SAR-derived ice motion in the Eastern Weddell Sea. Figure 5 shows two ERS-1 SAR swath cross-over locations near the WWGS '92 buoy array with the locations and times of the SAR frames listed, 'I'he six buoy starting locations are numbered and their drift trajectories indicated as dotted lines. Buoy motion between 02:08 GMT on 12 July and 09:49 GMT on 13 July is highlighted in solid, and SAR-derived ice displacement vectors are superimposed for the two periods separating each pair of SAR image frames in Fig. 5.

Sea ice drift speed and direction changes more rapidly in the Eastern Weddell Sea in response to the wind. Figure 5 SAR drift vectors show that during the early part of day 194, the northern part of the buoy array has a dominant eastward drift component, Subsequent

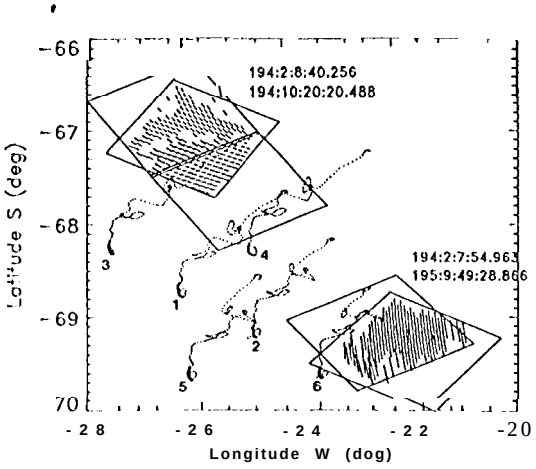

Figure 5. Eastern Weddell Sea ice motion at location b. in Fig. 1 (see Fig. 2b) on days 194 and 195 (12 and 13 July, 1992), together with WWGS '92 buoy drift tracks.

adjustment to a passing synoptic weather system is traced by the early loop in the buoy tracks. A seeond example of SAR ice motion near the south-eastern corner of the buoy array (with a 31 hour interval) indicates the change towards a more northerly drift direction. Corresponding buoy 6 data shown in Fig. 6a indicate; the distance travelled in each Argos buoy 3-hour sampling interval; the magnitude of the drift velocity; and the surface geostrophic wind (U_g). The early drift speed of buoy 6 on days 193-199 appears insensitive to the wind forcing until after day 197 when the drift direction changes to northeastward, Subsequent buoy 6 drift is more responsive to wind, with a stronger correlation between drift speed and U_x.

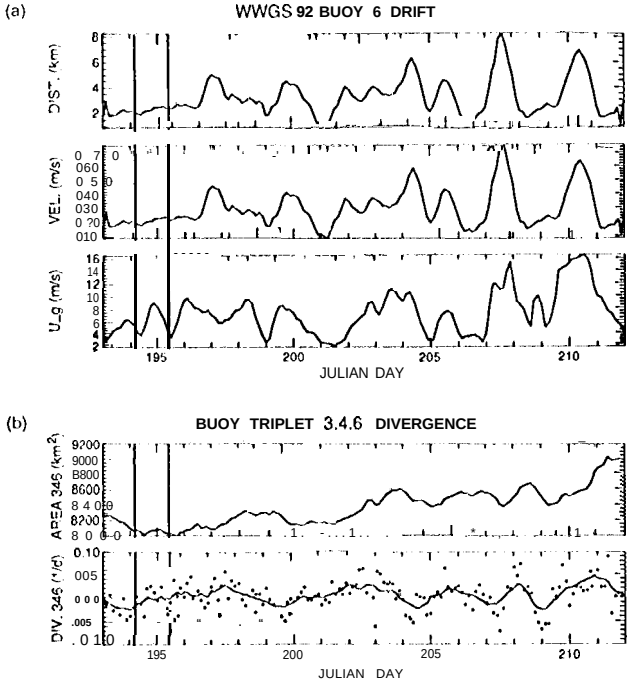

Figure 6. (a) Buoy 6 mean daily drift distance and velocity in reponse to geostrophic wind forcing (us); and (b) area change and divergence in buoy triangle 3. 4.6 during July 1992. In (b) 3 hourly divergences are shown as dots and the curve indicates the smoothed daily mean divergence.

Figure 6b shows the area and divergence derived from the relative locations of buoy triplet 3,4 and 6. At the start of July, onshore winds forced the ice against the shore, causing convergence and large internal ice stresses. The end of this period is reflected in Fig. 6b between days 193 and 194 as decreasing area and convergence. With a change of the synoptic situation on day 195, the ice begins to dilate and internal ice stresses are relieved. With the increase in area of triplet 3.4.6, buoy 6 becomes more responsive to the wind. After day 198 sea-ice drift more quickly reacts to pulses in U_g by ice divergence and lead formation. Low winds conversely result in relaxation events with convergence and lead closing,

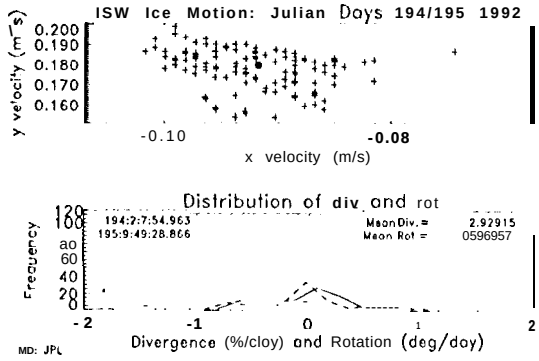

Figure 7. Ice velocity component distribution and accompanying histograms of the divergence (solid line) and rotation (dashed line) for the location shown in Fig. 5 and period indicated by vertical bars in Fig. 6

Figure 7 shows an example of SAR-derived velocity, divergence and rotation from the ice drift vector field in the south-east of Fig. 5. Corresponding buoy statistics are bracketed by vertical lines in Fig. 6 (marking the SAR image interval). The x and y components of the SAR velocity field indicate a mean magnitude of the drift velocity of 0.2 m/s (shown by a solid circle). Furthermore this value is almost identical with mean buoy 6 drift speed in Fig 6a for the same interval. In the lower panel of Fig. 7, histograms of the divergence (solid line) and rotation (dotted line) are plotted and the mean values listed. Due to the large variation in divergence and rotation at the mesoscale, the mean value in the SAR divergence histogram is not so representative of the divergence in buoy triplet 3.4.6. The median value of divergence of 0.27%/d is more representative of the daily values shown in Fig 6b.

The mean daily July divergence computed over the 20,000km^2 six-buoy array is 0.4±0.6%/day, but opening and closing of leads is spatially variable, Northwesternmost Argos drifters respond most sensitively to the mean surface geostrophic wind forcing and the total production of new ice in July is approximately 1, 100km^2, resulting from a mean divergence of 0.67*0.45%/day, Southeastern buoys tend to converge over this period, confirming significant spatial variability in the divergence over the buoy array, This large variance, on different scales, makes it imperative that SAR be employed to monitor regional differences in divergence and new icc production during winter.

IV. CONCLUSIONS

Our results demonstrate that SAR is equally as adept at tracking Southern Ocean sea ice as was previously demonstrated using Arctic ERS-1 data. Providing sampling locations and imaging times are carefully chosen, details of the ice kinematics field can be effectively characterised at the 100 km space scale. Buoy motion spectra indicate that the related time scale of 100 km examples of Antarctic ice motion is of the order of only a few hours. Examples show, therefore, that displacements over intervals of time do not always represent the true ice floe trajectories over the intervening period, as reflected by the ice camp and drifting buoys. Thus, it is necessary to obtain SAR image coverage as frequently as possible to overcome problems of aliasing ice motion trajectories and thus opening and closing "events" within the Southern Ocean sea-ice cover.

V. ACKNOWLEDGMENTS

MRD performed this work at the Jet Propulsion Laboratory, California Institute of Technology under contract to the National Aeronautics and Space Administration. Ron Kwok and Shirley Pang of JPL are sincerely thanked for their efforts in developing southern hemisphere geolocation and ice-tracking capability. ESA are gratefully acknowledged for)31{ -1 SAR acquisition planning and Jörg Gredel and the members of D-PAF for SAR product generation. This study was made possible by ESA support of PIPOR proposal PIP.Ant3.

VI. REFERENCES

Gordon, A.L. and Ice Station Weddell Group of Principal Investigators and Chief Scientists, Weddell Sea Exploration from Ice Station, *EOS*, 74, 11, 121-126, 1993.

Kwok, R., J.C. Curlander, R. McConnell, and S.S. Pang, An ice-motion tracking system at the Alaska SAR facility, *IEEE J. Oceanic Eng.*, *15*, 1,44-54, 1990.

Kwok, R., E. Rignot, B. Holt, and R. Onstott, An overview of the geophysical sca ice products generated at the Alaska SAR Facility, *J. Geophys. Res.*, 97, C2, 2391-2402,1991.